Journal of Solid State Chemistry 316 (2022) 123619

Contents lists available at ScienceDirect

Journal of Solid State Chemistry

journal homepage: www.elsevier.com/locate/jssc

Getting insight into how iron(III) oleate precursors affect the features of magnetite nanoparticles

Karam Nader [a], Idoia Castellanos-Rubio [a], Iñaki Orue [b], Daniela Iglesias-Rojas [a], Ander Barón [a], Izaskun Gil de Muro [a,c], L. Lezama [a], Maite Insausti [a,c,*]

[a] Dpto. Química Orgánica e Inorgánica, Facultad de Ciencia y Tecnología, UPV/EHU, Barrio Sarriena s/n, 48940, Leioa, Spain
[b] SGIker, Servicios Generales de Investigación, UPV/EHU, Barrio Sarriena s/n, 48940, Leioa, Spain
[c] BC Materials, Basque Center for Materials, Applications and Nanostructures, Barrio Sarriena s/n, 48940, Leioa, Spain

A B S T R A C T

The achievement of a successful heating power response of Fe_3O_4 nanoparticles for being applied in magnetic hyperthermia entails an exhaustive control of their magnetic characteristics and therefore, of the synthesis method employed. Despite the fact that one of the best wet-chemical methods to finely adjust Fe_3O_4 nanoparticles (NPs) size over 15 nm is the thermal decomposition of iron(III) oleate, the studies about the specific influence of iron(III) oleate precursor on the IONPs are particularly scarce. So, in this work five iron(III) oleate precursors have been systematically prepared varying synthesis conditions and it has been analyzed how their characteristics affect the features of the ulterior magnetite NPs. The refined synthesis method has yield monophasic and monodisperse NPs of magnetite (Fe_3O_4) with different sizes (in the 10–40 nm range) and morphologies (cuboctahedral, octahedral and spherical). A complete chemical, structural, morphological and magnetic characterization have been performed to correlate the properties of the iron(III) oleate with the features of the subsequent magnetite NPs.

1. Introduction

Magnetic iron oxide nanoparticles (IONPs) are highly biocompatible and versatile materials with structure dependent properties which can be properly tailored for applications in different fields, providing a basis for many key technologies [1,2]. These nanoparticles (NPs) are becoming promising building blocks in the biomedical field since they can act as contrast materials for diagnosis in magnetic resonance imaging (MRI), drug delivery carriers or therapeutic agents in magnetic hyperthermia. Specifically, for improving the magnetic hyperthemia performance it is necessary to achieve high values of saturation magnetization and suitable magnetic anisotropy, which entails an exhaustive control of the synthesis conditions in order to prepare good quality IONPs [3,4]. Most attempts have been focused on varying the typical parameters of the chemical synthesis (time, temperature, solvents, surfactants, molar ratios, etc.) to reduce crystal defects, obtain monophasic systems and tune the size and morphology of the NPs [5]. Recently, it has been observed that precise control over the shape of IONPs with sizes above the superparamagnetic limit (>20 nm) gives rise to an outstanding magnetic hyperthermia performance [6,7]. However, obtaining a fine control over the morphology of the IONPs while keeping size/shape monodisersity, high crystallinity and compositional homogeneity is quite challenging, a task that turns out to be even more demanding for magnetic NPs with sizes above 15 nm. In addition, the aggregation state increases with size which clearly affects the hyperthermia performance. Consequently, a great effort has been developed to understand the synthetic factors conditioning the structural characteristics of the final materials [8].

Although thermal decomposition of inorganic precursors provides the best approximation for formation of good quality magnetite nanoparticles, the nature of the iron precursors ($Fe(acac)_3$, pentacarbonyliron(0), iron(III) oleate, …), solvents (octadecene, benzyl ether, …) and surfactants (oleic acid, oleylamine) and the employed heating profile still lead high variability in the magnetic properties [9–11]. This fact is related to the difficulty in the control of iron oxidation state during the synthesis process, the evolution of Fe(III) species to Fe(II) species or the formation of radical intermediates and reactive monomer species [12].

It is noteworthy that the production of IONPs usually implies the formation of iron(III) oleate intermediate species, regardless of the precursor used; thus, a priori, a more simple and predictable synthetic pathway is obtained when iron(III) oleate precursors are initially decomposed [13,14]. Nevertheless, the composition and purity of the iron(III) oleate is the key factor for the preparation of NPs of iron oxides, and the iron sources employed, $FeCl_3$, $Fe(acac)_3$, FeO(OH), etc. also condition the iron intermediates turning ulterior nucleation and growth in different directions [15,16]. A recent study has shown that from Fe(II) and Fe(III) carbonates exclusively star-shaped nanocrystals of wüstite

* Corresponding author. Dpto. Química Orgánica e Inorgánica, Facultad de Ciencia y Tecnología, UPV/EHU, Barrio Sarriena s/n, 48940, Leioa, Spain.
E-mail address: maite.insausti@ehu.eus (M. Insausti).

https://doi.org/10.1016/j.jssc.2022.123619
Received 28 June 2022; Received in revised form 1 September 2022; Accepted 20 September 2022
Available online 29 September 2022

were obtained, which transformed to cubic-shaped NPs, despite the iron source employed [17]. In the last years, several strategies have been carried out in order to avoid wüstite formation within IONPs, such as oxidation during, post synthetic process or esterification-mediated reactions at lower temperatures to avoid the over-reduction of iron, … [14,18,19]. However the attainment of reliable correlations between iron precursors and the produced IONPs requires further consistent studies.

Therefore, this work aims to contribute to this topic by systematically synthesizing iron(III) oleate precursors varying the synthesis conditions and analyzing how their chemical properties affect the features of the ulterior Fe_3O_4 nanoparticles. A complete chemical, structural, morphological and magnetic characterization have been performed to finally discuss the role of the different parameters in the improvement of the prepared magnetite NPs. These nanomaterials have also been characterized by electron magnetic resonance spectroscopy (EMR) which provide additional information about dipolar interactions and magnetic behavior both in solution and deposited on a paper.

2. Experimental section

2.1. Materials

Sodium oleate was purchased from TCI. Iron (III) chloride hexahydrate, hexane and chloroform were obtained from Sigma Aldrich. Oleic acid (90%), 1-octadecene (90%), benzyl ether (98%) and oleylamine were purchased from Sigma-Aldrich and used as received without purification. Sodium oleate ($NaC_{18}H_{33}O_2$) was obtained from TCI America (97%) and ethanol and tetrahydrofuran (THF) from Panreac S.A. and Emplura, respectively.

2.2. Preparation of iron(III) oleates

Different amounts of $FeCl_3{\cdot}6H_2O$ and sodium oleate ($NaC_{18}H_{33}O_2$) were mixed with hexane (140 mL), ethanol (80 mL) and distilled water (60 mL) in a three neck round bottom flask (Table 1 and Table S1). The reaction mixture was maintained under N_2 flux and mechanical stirring for 20 min. After that, it was heated up to 60°C at 5 °C/min and held at reflux during 1 h. Subsequently, the mixture was cooled down, transferred to a separatory funnel and washed with water (3 x 100 mL). Then, the organic phase was separated and transferred into a beaker to evaporate the remaining solvents at 110 °C during different drying periods to ensure the complete removal of ethanol, hexane and water, resulting in brown-reddish waxy solids. Iron(III) oleates were named as FeOL_X, X = A, B, C, D, E depending on the synthesis conditions.

2.3. Preparation of Fe_3O_4 nanoparticles

Previously synthesized iron(III) oleate (4.5 g, 10 mmol) was added to a mixture of octadecene (10 mL), benzyl ether (5 mL) and the corresponding surfactant, oleic acid (10 mmol) or oleylamine (30 mmol), in a three neck round bottom flask under N_2 flux, keeping sealed to ensure no leaking (Table 1). The reaction mixture was heated up to 190 °C with a temperature ramp rate of 10 °C/min and then to 330°C at 3 °C/min, while mechanical stirring, as previously explained in our previous work [20]. The system was held under reflux for 1 h and cooled down to room temperature. The black powder obtained was cleaned by centrifugation at 22000 rpm (50 min at 6 °C) by adding 10 ml THF and 20 ml ethanol. After repetition of the process, they were dispersed in 15 ml chloroform and stored in the fridge. In relation with the oleate precursor used in the synthesis, nanoparticles were named as follows Fe_3O_4_X (X = A, B, C, D, E) and in the case of the synthesis performed in the presence of oleylamine, Fe_3O_4_F.

2.4. Characterization of Fe(III) oleates and Fe_3O_4 nanoparticles

Elemental analysis of the $Fe(oleate)_3$ precursors were carried out on a Euro EA Elemental Analyzer (CHNS) from Eurovector and iron content on a Horiba Yobin Yvon Active Atomic Emission Spectrometer after acid digestion (1100 μL H_2SO_4 and 400 μL H_2O_2) of the samples. FTIR characterization was performed in the 400-4000 cm^{-1} by Fourier transform using the FTIR- 8400S Shimadzu spectrometer. The amount of organic mass coating the nanoparticles was determined by thermogravimetric analysis in the 20–900 °C temperature range, in Ar atmosphere with the NETZSCH STA 449C equipment. X-ray diffractograms were collected in a Panalytical X'Pert PRO diffractometer with Bragg-Breton geometry by using CuKα radiation (40 kV and 40 mA). The diffractograms were collected in the $5° < 2\theta < 90°$ range with a step size of 0.026° and scan step speed of 1.25s. TEM images were obtained with a Philips CM200, EDX and WDX microanalysis equipment on a single slope sample holder at 200 kV and a point resolution of 0.235 nm. To prepare the samples, 10 μL of the stock solution was diluted in 1.5 mL of $CHCl_3$ and a drop was deposited on a small Cu grid with a carbon film. Magnetization measurements as a function of magnetic field and temperature were carried out on the SQUID magnetometer (MPMS3, Quantum Design model). Magnetization at RT and 5 K was obtained from the dried samples as powder, normalized per unit mass of Fe_3O_4 and M(T) measurements were performed in diluted stock solutions (1 mg mL^{-1}) deposited on a filter paper to minimise magnetic interaction. EMR spectra were carried out at RT on solution and solid samples using a Bruker ELEXSYS E500 spectrometer operating at the X-band. The spectrometer was equipped with a super-high-Q resonator ER-4123-SHQ, the magnetic field was calibrated by a NMR probe and the frequency inside the cavity (~9.36 GHz) was determined with an integrated MW-frequency counter.

3. Results and discussion

Fe_3O_4 nanoparticles of different sizes have been synthesized from five $Fe(oleate)_3$ precursors, which have been prepared varying $FeCl_3$:NaOleate molar ratio and the drying period to stabilize the precursor (annealing time) (Table 1). These oleate precursors have been characterized by chemical analysis and infrared spectroscopy (Table S1 and Table 1).

Concerning the composition of the iron(III) oleates, elemental analysis and iron analysis suggest a relation Ol:Fe lower than 3 for most of the cases (except for FeOL_E), probably due to H_2O molecules, impurities of other counterions in the samples or to a small presence of Fe(II) ions

Table 1
$FeCl_3$:NaOleate molar ratio used in the synthesis of the precursor and annealing time (h) for precursor stabilization. Δ_1 and Δ_2 ($\nu_{asym} - \nu_{sym}$) difference between asymmetric and symmetric $\nu(COO^-)$ bands of $Fe(oleate)_3$ precursors in Fig. 1. Surfactant type (OA, oleic acid and OAm, oleylamine) and amount used in the synthesis of the Fe_3O_4 NPs. Ligand amount surrounding the NPs (TGA %), crystallite size (D_{XRD}) calculated by Scherrer equation and particle size obtained by TEM (D_{TEM}).

SAMPLE	Precursor	$FeCl_3$:NaOl (mmol)	Annealing t (h)	Δ1 (cm-1)	Δ2 (cm-1)	Surfact.(mmol)	TGA %	D XRD ±σ (nm)	D TEM ±σ (nm)
Fe_3O_4_A	FeOl_A[a]	40:120	Intense (21)	83	150	OA (10)	21.6	20.8±1.1	17.7±2.6
Fe_3O_4_B	FeOl_B	40:120	Light (21)	89	145	OA (10)	18.8	43.5±2.5	36.4±2.5
Fe_3O_4_C	FeOl_C	40:120	Light (42)	81	147	OA (10)	23.4	38.1±2.1	32.2±3.4
Fe_3O_4_D	FeOl_D	40:115	Light (21)	72	141	OA (10)	29.6	42.0±1.7	36.2±3.3
Fe_3O_4_E	FeOl_E	40:125	Light (21)	83	141	OA (10)	31.6	31.1±1.7	26.0±3.5
Fe_3O_4_F	FeOl_D	40:115	Light (21)	72	141	OAm(30)	11.8	16.2±0.9	12.6±2.3

[a] fast pre-annealing step.

(Table S1) [15]. Sample FeOL_E has been the only one where an excess of sodium oleate (125 mmol) has been employed.

The characteristics of the precursor, a non-crystalline brown gel, can lead to different configurations of the iron-carboxylate complex (ionic, unidentate, bridging and bidentate) [21]. This information has been obtained from the separation ($\Delta = \nu_{asym}$-ν_{sym}) of the $\nu_{asym}(COO^-)$ and $\nu_{sym}(COO^-)$ vibrational modes observed in FTIR spectra (Fig. 1 and Fig. 1S). For separations lower than 110 cm^{-1} a bidentate coordination is expected, for $\Delta > 200$ cm^{-1} an unidentate ligand and between 110 and 200 cm^{-1} a bridging coordination can be deduced [22]. To calculate Δ values the band splitting has been considered and the minimum Δ_1 and maximum Δ_2 values have been obtained, which are indicative of both bidentate and bridging coordination in all the samples (Table 1), in spite of the drying times employed. Increasing drying time (42 h) for FeOL_C does not influence the type of coordination. Both modes of coordination yield homogeneous distribution of cations in the oleates, and so, homogeneous decomposition which provides a wide thermal window between the dissociation of the weakly linked ligands (formation of the nuclei) and the dissociation of the tidily ones (growth), ensuring the formation of similar nuclei growing into uniform nanoparticles [5]. Together with this, a strong band assigned to the C=O group of non-coordinated or weakly coordinated oleic acid can also be observed, which is more intense in the case of FeOL_A and FeOL_E (Fig. 1). This last sample also presented a stoichiometric relation of oleate ligand with respect to iron(III) because of the excess of sodium oleate used in the synthesis, 125 mmol, (see Table 1). The FTIR spectra in the 4000–400 cm^{-1} range are displayed in Fig. S1 in the Supporting Information.

These iron(III) oleates were mixed with a surfactant (10 mmol oleic acid) in the presence of octadecene and dibenzyl ether, except for the preparation of Fe_3O_4_F where 30 mmol of oleyalmine were used, and after thermal treatment six different magnetite samples were obtained (Table 1). X-ray diffraction patterns of the samples, both peak positions and intensities, match well with the inverse spinel structure (S.G. Fd-3m, PDF 089–0691) [23], without detectable presence of impurities as wüstite or other iron oxide phases. Small intensity peaks around 30° correspond to crystallized octadecene which remains precipitated if the sample has not been sufficiently cleaned (* marked in Fig. 2). The adequate relation of surfactant and ligands, in a mixture of solvents with a proper redox balance (see Experimental Section), have been chosen considering previous experience and it has led to crystalline phase of magnetite in all cases [20,24]. Deconvolution of (3 1 1) diffraction peak has been used to calculate crystallite sizes of the particles by means of

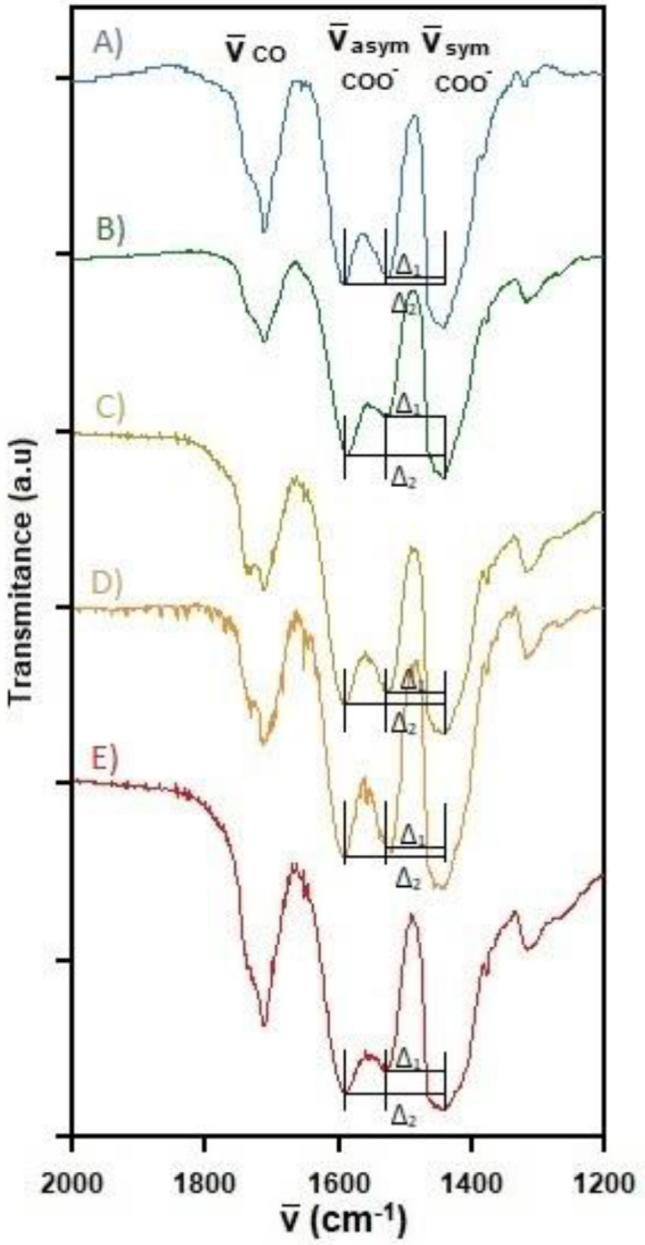

Fig. 1. FTIR spectra of iron(III) oleate complexes: FeOl_A, FeOl_B, FeOl_C, FeOl_D, FeOl_E. Evolution of (C=O) band, $\nu_{asym}(COO^-)$ asymmetric and $\nu_{sym}(COO^-)$ symmetric and Δ ($\nu_{asym} - \nu_{sym}$). The FTIR spectra in the 4000–400 cm^{-1} range are displayed in **F**igure S1 in the Supporting Information.

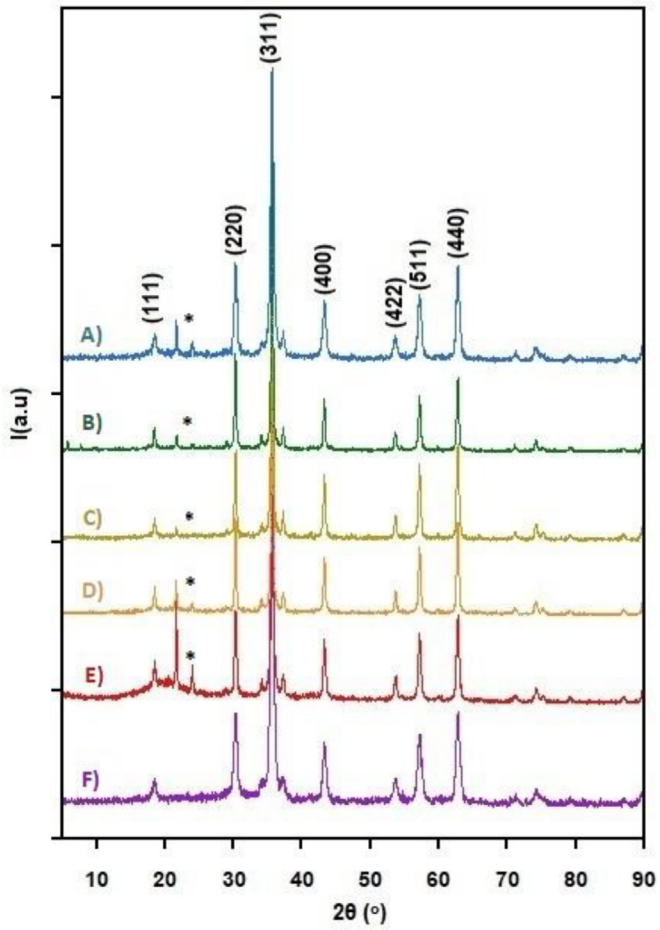

Fig. 2. X-ray powder diffraction patterns of magnetite samples synthesized from iron oleate precursors: Fe_3O_4_A, Fe_3O_4_B, Fe_3O_4_C, Fe_3O_4_D, Fe_3O_4_E. *Peaks corresponding to crystallized octadecene.

Scherrer's equation (Table 1, Table S2). These sizes vary from 16.2 ± 0.9 to 43.5 ± 2.5 nm and are similar to those observed by microscopic measurements, as will be explained later on. The smallest size corresponds to Fe_3O_4_F (12.6 ± 2.3), the nanoparticles synthesized in the presence of oleylamine that is competing with the oleate molecules coming from the iron oleate precursor in attaching the nuclei, and due to its large concentration (30 mmol, see Table 1) it hinders the progressive growth of the nuclei [25].

The amount of organic matter coating the nanoparticles has been calculated from gradual thermal decomposition with temperature (Fig. S2). Two huge steps can be observed in the decomposition curves, one in the 300-400 °C range where ligands decompose or evolve to a residue mainly formed by oleates firmly attached to iron and intermediate iron carbonates and the other one around 750 °C to yield a residue formed from evolution of the magnetite core to a mixture of iron oxides, as has been previously observed [26]. Weight losses vary from 11% to 31%, more related with the cleaning process of the nanoparticles than with the logical relation organic matter/surface area. Despite it was expected more ligands attached to the smallest NPs which present the highest surface/volume ratio, no such correlation was visualized, surely due to the less affinity of an aminated ligand to iron atoms in comparison with carboxylate ligand such oleic acid. It is worthy to mention that samples with a very low content of organic matter (Fe_3O_4_A and E) are those with the most intense $\nu_{C=O}$ band, indicating that weakly attached or free ligands are more easily lost in a cleaning process and oleates forming bridging and bidentate intermediate more easily could evolve to surface coating ligands, being maintained in the cleaning process.

Fig. 3 illustrates the morphological evaluation performed by Transmission Electron Microscopy (TEM) of the samples together with the corresponding size distributions. Among the samples synthesized with only oleic acid, Fe_3O_4_A is the smallest one (D = 17.7 ± 2.6 nm) and it presents the highest polydispersity together with an octahedral morphology with different truncations. Samples with fairly well-defined octahedral morphology are Fe_3O_4_B, Fe_3O_4_C and Fe_3O_4_D, showing mono-dispersity ($\beta_{TEM} \leq 10\%$) and similar sizes between 32 and 36 nm. In the case of Fe_3O_4_E particles, homogeneous cuboctahedral morphology is observed. Finally, Fe_3O_4_F sample size is small (D = 12.6 ± 2.3 nm) with spherical nanoparticles and with the highest polydispersity index ($\beta_{TEM} = 18\%$). These morphologies can be related with the characteristics of the iron oleate precursors (position and intensity of the ν_{COO} bands in infrared spectroscopy). Samples with less amount of free ligand show more defined morphologies, in particular octahedral. Precursors with more strongly coordinated oleates (bridging and bidentate) evolve to octahedral morphologies. In this case, (111) planes of the magnetite structure are favoured due to their higher planar density; since more ligands are attached to (111) planes, the more reactive (100) planes tend to grow to extinction (Fe_3O_4_B, Fe_3O_4_C and Fe_3O_4_D samples in Fig. 1) [27]. It is worth mentioning that an increase of the annealing time in the preparation of the iron(III) oleate precursor (see Table 1) causes the nano-octahedra to grow to less extent (Fe_3O_4_C). However, in the cases of precursors that content an excess of free ligands (ν_{COO} band at 1700 cm^{-1}), the steric barrier around the (100) and (111) faces nearly equalises giving rise to more faceted morphologies such as the cuboctahedron (Fe_3O_4_E) or truncated octahedra (Fe_3O_4_A). Finally, for Fe_3O_4_F sample, the excessive amount of oleylamine in the synthesis, with less affinity for iron, hampers the growth of any particular face and spherical morphologies and small sizes are obtained. The effect of the annealing time of the iron oleate can also be noticed in the smaller size of Fe_3O_4_C sample, comparing with the other octahedral NPs (see Table 1 and Table S1). Longer times reinforces metal-ligand coordination which leads to a higher nucleation temperature, and hence a smaller size. It is noteworthy that morphological sizes match rather well with crystalline sizes, although TEM sizes are slightly smaller than DRX sizes, corroborating the presence of single crystals in the nanoparticles and the lack of twinned crystal, that usually appear from iron oleate precursors [15].

Magnetization measurements (M(H) and M(T)) were performed

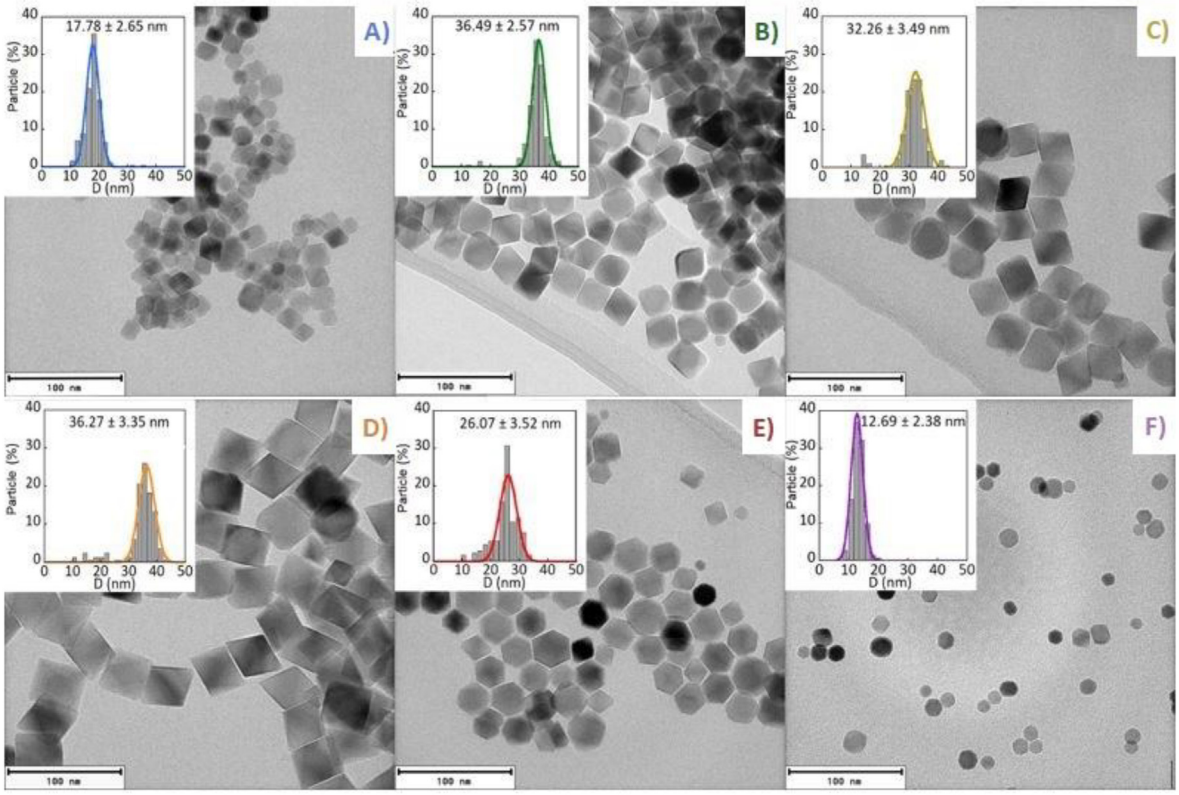

Fig. 3. TEM micrographs and corresponding size distributions of as-synthesized magnetite samples: A) Fe_3O_4_A, B) Fe_3O_4_B, C) Fe_3O_4_C, D) Fe_3O_4_D, E) Fe_3O_4_E, F) Fe_3O_4_F. Scale bars 100 nm.

between 5 and 300 K and are represented in Figs. 4 and 5. Data of saturation magnetization, M_S, coercive field, H_c, and reduced remanent magnetization M_r/M_s, are summarized in Table 2. The ferromagnetic character of the samples can be gathered by the presence of hysteresis at RT for all samples except Fe_3O_4_F. The values of H_c at 5 K, vary among 42–62 mT, typical of this kind of Fe_3O_4 nanoparticles with sizes >20 nm [28]. In the case of Fe_3O_4_F, it presents H_c values close to 0 at R.T., characteristic of a superparamagnetic behaviour of samples with sizes near or below the superparamagnetic limit. The saturation magnetization values of the whole set of samples at RT are in the range of 85–90 Am^2/kg and at 5 K from 91 to 99 Am^2/kg, which are very close to those of bulk magnetite (92 and 98 Am^2/kg, at RT and 5K, respectively). These values are representative of the high purity and quality of the crystals, with no significant effects of magnetic ordering disturbances caused by surface effects. These characteristics together with a suitable magnetic anisotropy of the synthesized nano-octahedra (Fe_3O_4_B, Fe_3O_4_C and Fe_3O_4_D) results in enlarged dynamical hysteresis loop area, and thus, enhanced heating capacity in magnetic hyperthermia. In addition, the thermal dependence of M_s values also matches well with that of stoichiometric magnetite (6%), discarding the presence of vacancies of Fe^{2+}/Fe^{3+} in most of the samples, a common drawback that is difficult to overcome because of the inherent complexity of the reaction pathways [7,29]. The shape of hysteresis cycles at 5 K fit well with the model of Stoner-Wohlfarth; in fact, the reduced remanence values (M_r/M_s) of most of samples are very close to the 0.5 value predicted by this model for uniaxial single domains without magnetic interactions between particles (Table 2) [30].

The purity and high quality of the prepared Fe_3O_4 nanocrystals can also be corroborated by the step like characteristic of the ZFC-FC curves (Fig. 5). The sharp increase in the magnetization is due to an increase in the magnetic anisotropy because of the transition from a cubic lattice at high temperature to a monoclinic one around 120 K (Verwey transition, T_v). At low temperatures, the orthorhombic elongation of the lattice leads to the large uniaxial magnetocrystalline anisotropy and the sharp change in the magnetic curves. The position of the T_v also can also give information about the stoichiometry of the samples, specifically the Fe^{2+}/Fe^{3+} relation in magnetite [31]. To compare this effect in the Fe_3O_4 A-F set of samples, the derivative of the magnetization against temperature has been calculated and maxima have been included in Table 2. The octahedral and homogeneous Fe_3O_4_B, Fe_3O_4_C and Fe_3O_4_D nanoparticles present Verwey temperatures very close to the 120 K value of stoichiometric bulk magnetite, fact that corroborates the crystallinity of magnetite NPs and excellent quality of these nano-octahedra. However, displacements to lower temperatures are observed for the smallest nanoparticles (Fe_3O_4_A, Fe_3O_4_F) and for Fe_3O_4_E, which are indicative of a decrease of Fe^{2+}/Fe^{3+} relation within the magnetite phase, probably due to the presence of vacancies in the structure. Additionally, the lower Tv in A, E and F nanoparticles could also be related to surface spin disorders that are more easily arisen in small nanoparticles. Therefore, both the Fe^{2+} vacancies within the crystal structure and the possible surface effects are responsible for the lower saturation magnetization values in A, E and F samples (Table 2) [20]. Regarding the shape of the ZFC-FC curves in Fe_3O_4_F sample, it resembles those of the superparamagnetic nanoparticles with blocking temperatures below RT (~280 K), an inference that was previously drawn by the absence of coercivity in M(H) (Fig. 4).

The coercivity and the M_R/M_S relation have also been studied as a function of temperature to elucidate the influence of the size and shape of the NPs on the magnetic behavior (Fig. 6). In all the samples, both reduced remanent magnetization and coercivity decrease with increasing temperature with an abrupt change near the T_v transition. Nevertheless, the evolution with temperature is different from one sample to another. Nanoparticles with octahedral morphology and M_s and T_v values coincident with those of bulk magnetite (Fe_3O_4_B, Fe_3O_4_C and Fe_3O_4_D) present an abrupt jump at T_v and smooth evolution of H_c and M_S at lower and higher temperatures. In the case of Fe_3O_4_A and Fe_3O_4_E samples a progressive decrease of the values is observed with a smooth change around T_V. Finally, for the smallest one (Fe_3O_4_F) that present superparamagnetic behavior, the Hc and Mr/Ms values steadily decrease with temperature. It is to note that coercivity is influenced by the anisotropy energy, that is, by the magnetic anisotropy constant (K) and the volume of the NPs (V); thus for more anisotropic NPs with larger sizes the corresponding M(H) curves should contain wider hysteresis. At this point it should be highlighted that previous studies have shown that the octahedral morphology in magnetite NPs produces larger shape anisotropy than other more commonly obtained morphologies such as spherical, cubic and cuboctahedral [20]. Thus, Fe_3O_4–B, C and D samples composed of octahedral NPs with the average dimensions in the 38–42 nm range present larger H_c values in the whole range of temperatures, from 5 K to 300 K, being really important that these samples present quite large Hc values at RT, a feature that would bring on large hysteresis areas in AC measurements, as long as the dipolar interactions among NPs are minimized. In consequence, Fe_3O_4_B, C and D present, a priori, a great potential to carry out efficient antitumoral magnetic hyperthermia treatments.

Finally, Electron Magnetic Resonance (EMR) has been employed to fulfill the contributions of internal magnetization of the samples, as EMR is a powerful technique for both superparamagnetic and ferromagnetic systems (Fig. 7). The measurements have been performed in colloidal dispersions of chloroform after vigorously shaking the solutions for 5 min to avoid the lack of reproducibility observed in spectra of solid samples. The signals appearing in Fig. 7 are asymmetric and broad and in some cases, different contributions are observed. Despite the difficulty in calculating the g_{eff} values due to the asymmetry of the curves, a clear evolution of the resonance field, H_r (estimated from the maxima and the

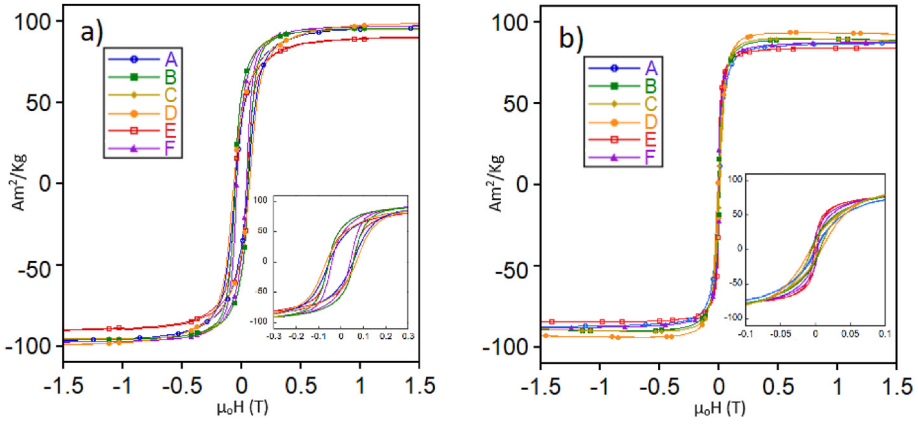

Fig. 4. Magnetization versus magnetic field curves of the magnetite samples obtained from iron(III) oleate precursors: Fe_3O_4_A, Fe_3O_4_B, Fe_3O_4_C, Fe_3O_4_D, Fe_3O_4_E and Fe_3O_4_F. **a)** 5 K and **b)** 300 K. The insets show an enlarged view of the low field region.

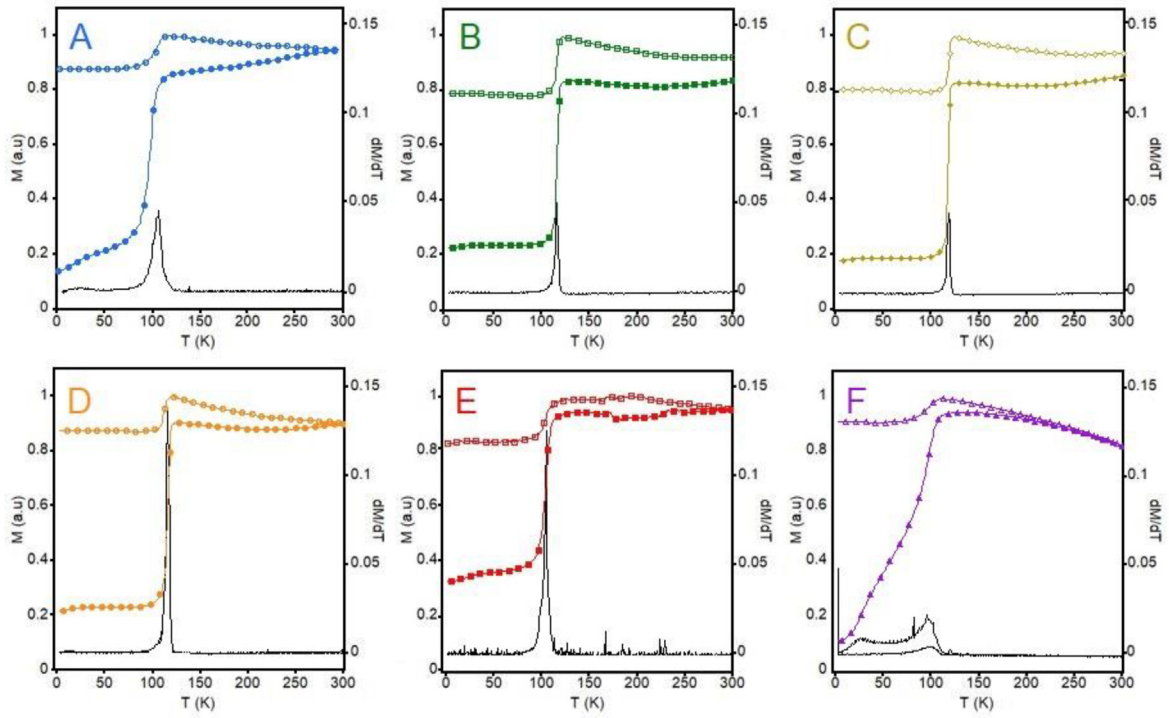

Fig. 5. Magnetization as a function of temperature measured in ZFC (solid markers) and FC modes (open markers) of samples together with derivatives of ZFC magnetization (black lines) of magnetite samples obtained from iron(III) oleate precursors: Fe_3O_4_A, Fe_3O_4_B, Fe_3O_4_C, Fe_3O_4_D, Fe_3O_4_E and Fe_3O_4_F.

Table 2
Data of nanoparticle sizes obtained from XRD, saturation magnetization (M_S), coercivity (H_c) and reduced remanence (M_r/M_S) at RT and 5 K and Verwey transition temperature (T_v) of the whole set of Fe_3O_4 nanoparticles.

SAMPLE	XRD **D (σ)**(nm)	**M_S at RT (Am^2/kg_{inor})**	**M_S at 5K (Am^2/kg_{inor})**	**H_c at RT (mT)**	**H_c at 5K (mT)**	M_r/M_s 300 K	M_r/M_s 5 K	T_v (k)
Fe_3O_4_A	20.8 ± 1.1	88 [2]	97 [2]	0.9 [1]	52.0 [1]	0.02 [2]	0.39 [2]	107 [1]
Fe_3O_4_B	43.5 ± 2.5	90 [2]	96 [2]	6.6 [1]	61.7 [1]	0.23 [2]	0.45 [2]	117 [1]
Fe_3O_4_C	38.1 ± 2.1	90 [2]	96 [2]	5.3 [1]	61.4 [1]	0.19 [2]	0.44 [2]	118 [1]
Fe_3O_4_D	42.0 ± 1.7	94 [2]	99 [2]	11.3 [1]	62.3 [1]	0.18 [2]	0.45 [2]	117 [1]
Fe_3O_4_E	31.1 ± 1.7	85 [2]	91 [2]	1.3 [1]	53.0 [1]	0.09 [2]	0.49 [2]	107 [1]
Fe_3O_4_F	16.2 ± 0.9	88 [2]	97 [2]	0	42.4 [1]	0	0.47 [2]	97 [1]

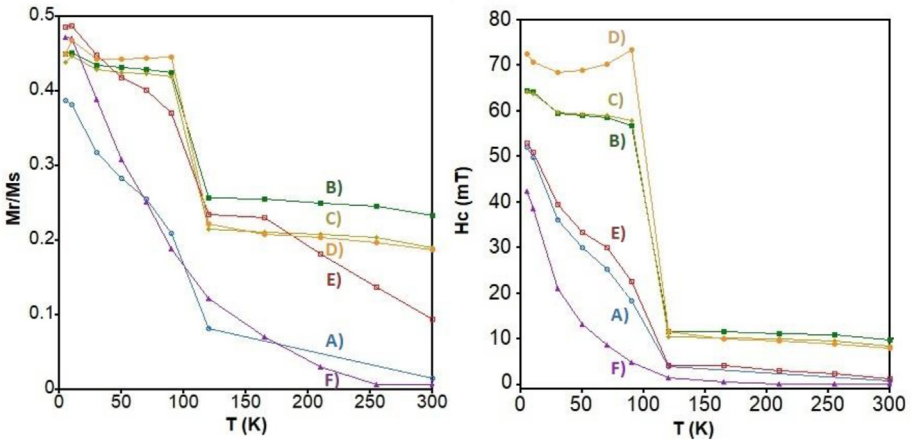

Fig. 6. a) Coercivity (H_c) and (b) reduced remanence (M_r/M_S) as a function of temperature of magnetite samples: Fe_3O_4_A, Fe_3O_4_B, Fe_3O_4_C, Fe_3O_4_D, Fe_3O_4_E and Fe_3O_4_F.

zero crossing of the absorption derivative) is observed from one sample to another. Nevertheless, in all cases g values are above 2.122 which corresponds to the alignment of crystalline magnetite along the easy axis, meaning that through this technique all the samples (even Fe_3O_4_F sample) are perceived as ferromagnetic, note that the time window for an EPR measurement is lower than for DC Magnetometry [32]. The H_r field

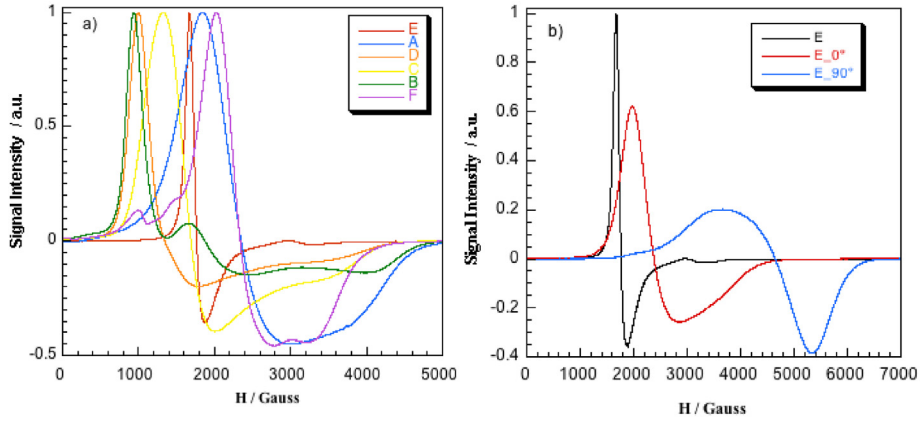

Fig. 7. a) Room-temperature EMR spectra of the magnetite samples at random: A) Fe_3O_4_A, B) Fe_3O_4_B, C) Fe_3O_4_C, D) Fe_3O_4_D, E) Fe_3O_4_E and F) Fe_3O_4_F. b) Spectra of Fe_3O_4_E sample deposited on an acetate film measured in plane ($\theta = 0°$) and out of plane ($\theta = 90°$). The measurements at $\theta = 0°$ and $\theta = 180°$ of Fe_3O_4_A, B, C, D, F can be found in Fig. S3 of the Supporting Information.

depends on the alignment of the nanoparticles towards the external magnetic field, that is, on the internal field of the nanoparticles that increases with the size and anisotropy (shape and surface) of the particles [33]. The H_r of our set of magnetite samples are arranged in increasing order as follows: Fe_3O_4_B < Fe_3O_4_D < Fe_3O_4_C < Fe_3O_4_E < Fe_3O_4_A < Fe_3O_4_F, a trend that matches well with the decreasing sizes observed for the nanoparticles (Table 2).

The signals of the majority of the NPs are asymmetric with an intense peak at lower fields due to the alignment towards the external magnetic field. In the case of the octahedral NPs (Fe_3O_4_B, Fe_3O_4_D, Fe_3O_4_C) the peaks are narrower, which denotes that these samples present very low polydispersity. It is to note the shape of the spectrum of Fe_3O_4_E (Fig. 7a), where a very narrow signal is observed, denoting a high homogeneity in the resonant field values for all the particles of the sample. This fact implies not only a low dispersity of sizes but also the absence of intense dipolar interactions among the particles that could give rise to the formation of aggregates or hinder the alignment of the particles with the applied field. The symmetry of the morphology, cuboctahedral nanoparticles, together with the large amount of organic matter coating the nanoparticles (see Table 1) seems to be the reason for the lack of interactions. Actually, at high resonant fields only a weak contribution could be observed in Fe_3O_4_E sample. In the case of the Fe_3O_4_A and Fe_3O_4_F samples, the spectra are quite broad evidencing the difficulty of orientation of the particles with the field. This fact is usually related to the dispersity of sizes or morphologies of the nanoparticles along with the presence of agglomerates. Taking into account the TEM study, the samples with less defined facets and larger dispersion of sizes are Fe_3O_4_A and Fe_3O_4_F, and as it can be observed in Fig. 7 and Fig. S3, these features clearly influence the shape of the spectra (Fig. 3).

In order to gain a better insight into the influence of the magnetic dipolar interactions of these nanomaterials, NPs suspensions have been deposited on an acetate film and the EMR spectra have been recorded with the applied field parallel ($\theta = 0°$ orientation) and perpendicular ($\theta = 90°$) to the film plane. The spectra Fe_3O_4_E together with the spectrum of the sample in solution is shown in Fig. 7a and the spectra of both orientations for all the samples have been displayed in Fig. S3. In all cases, the EMR signals shift towards higher fields than those observed for the samples dispersed in chloroform, even for measurements made with the applied field parallel to the plane of the sample. This fact implies that dipolar interactions become more significant and the nanoparticles aggregate gently over time as the solvent starts evaporating. The Fe_3O_4_B, Fe_3O_4_C, Fe_3O_4_D and Fe_3O_4_E nanoparticles, which present sizes in the 31–43 nm range, show wider differences between the resonant fields in both directions, indicating higher magnetic interactions between particles. The strength of the interactions diminishes for smaller sizes, that is Fe_3O_4_A and Fe_3O_4_F nanoparticles, as it could be expected [34].

4. Conclusions

Five iron(III) oleates have been synthesized changing the Fe:NaOleate molar ratio and the annealing time for solvents removing. Next, Fe_3O_4 nanoparticles have been synthesized from these oleate precursors and the effects that the precursor features have on the ulterior magnetite NPs have been analyzed. In all the cases, monophasic and single crystals of magnetite with a narrow size distribution have been obtained. It has been observed that precursors synthesized with Fe:Oleate ratio $\leq$3 give rise to well-faceted nano-octahedra and sizes among 32 and 36 nm and with a very good shape/size homogeneity. It has also been observed that a larger annealing time in the synthesis of the precursor brings on smaller octahedral nanoparticles. Additionally, the samples composed of octahedral NPs display a saturation magnetization (Ms) and a Verwey temperature (Tv) similar to bulk magnetite. In addition, these octahedral samples have given rise to large coercivity values at RT. These characteristics, high quality NPs with high saturation magnetization together with a more suitable magnetic anisotropy are the key factors to obtain efficient magnetothermal actuation for being applied as agents for magnetic hyperthermia. Otherwise, when the precursors are synthesize using Fe:Oleate relation >3 the resulting nanoparticles present a cuboctahedral morphology and a magnetite phase with few Fe^{2+} vacancies, which involves a slight decrease in the Ms and Tv of the NPs. On the other hand, when the synthesis of the magnetite NPs is carried out with large amounts of oleylamine the resulting samples present a lower average dimension (~12 nm), spherical morphology, larger polydisersity of sizes and a superparamagnetic behavior. Finally, the EMR study has shown that octahedral particles show narrower peaks, which corroborates the good monodispersity and suitable features of these kind of nanosystems. To sum up, a proper control of the reaction conditions of iron oleate precursors is essential to reach high quality Fe_3O_4 nanoparticles with excellent magnetic properties and great potential for therapeutic magnetothermal applications.

CRediT authorship contribution statement

Idoia Castellanos-Rubio: Methodology. **Maite Insausti:** Writing – review & editing. **Iñaki Orue:** Magnetic characterization. **Daniela Iglesias-Rojas:** oleates preparation, MvsH measurements (RT). **Ander Barón:** oleates preparation, MvsH measurements (RT). **Izaskun Gil de Muro:** TEM measurements. **L. Lezama:** EMR characterization.

Declaration of competing interest

The authors declare that they have no known competing financial interests or personal relationships that could have appeared to influence

the work reported in this paper.

Data availability

No data was used for the research described in the article.

Acknowledgements

This work was supported by institutional funding from the Basque Government under IT1546-22 and from the Spanish Ministry of Economy and Competitiveness under PID2019-106845RB-100 project. We acknowledge the technical and human support provided by SGIker (UPV/EHU).

Appendix A. Supplementary data

Supplementary data to this article can be found online at https://doi.org/10.1016/j.jssc.2022.123619.

References

[1] E.M. Materón, C.M. Miyazaki, O. Carr, N. Josh, P.H.S. Picciani, C.J. Dalmaschio, F. Davis, F.M. Shimizu, Magnetic nanoparticles in biomedical applications: a review, Appl. Surf. Sci. Advances 6 (2021), 100163.

[2] C. Döpke, T. Grothe, P. Steblinski, M. Klöcker, L. Sabantina, D. Kosmalska, T. Blachowicz, A. Ehrmann, Magnetic nanofiber mats for data storage and transfer, Nanomaterials 9 (1) (2019) 1–12.

[3] B. Pelaz, C. Alexiou, R.A. Alvarez-Puebla, F. Alves, A.M. Andrews, S. Ashraf, L.P. Balogh, L. Ballerini, A. Bestetti, C. Brendel, S. Bosi, M. Carril, W. Cw Chan, C. Chen, X. Chen, X. Chen, Z. Cheng, D. Cui, J. Du, C. Dullin, A. Escudero, N. Feliu, M. Gao, M. George, Y. Gogotsi, A. Grunweller, Z. Gu, N. J Halas, N. Hampp, R. K Hartmann, M.C. Hersam, P. Hunziker, Ji Jian, X. Jiang, P. Jungebluth, P. Kadhiresan, K. Kataoka, A. Khademhosseini, J. Kopecek, N. A Kotov, H. F Krug, D. Soo Lee, C.-M. Lehr, K.W. Leong, X.-J. Liang, M. Ling Lim, L. M Liz-Marzán, X. Ma, P. Macchiarini, H. Meng, H. Mohwald, P. Mulvaney, A. E Nel, S. Nie, P. Nordlander, T. Okano, J. Oliveira, T. Hyun Park, R. M Penner, M. Prato, V. Puntes, V. M Rotello, A. Samarakoon, R. E Schaak, Y. Shen, S. Sjoqvist, A.G. Skirtach, M.G. Soliman, M. M Stevens, H.-W. Sung, B. Zhong Tang, R. Tietze, B. N Udugama, J.S. VanEpps, T. Weil, P.S. Weiss, I. Willner, Y. Wu, L. Yang, Z. Yue, Q. Zhang, Q. Zhang, X.- En Zhang, Y. Zhao, X. Zhou, W.J. Parak, Diverse applications of nanomedicine, ACS Nano 11 (3) (2017) 2313–2381.

[4] J. Huang, L. Bu, J. Xie, K. Chen, Z. Cheng, X. Li, X. Chen, Effects of nanoparticle size on cellular uptake and liver MRI with PVP-coated iron oxide nanoparticles, ACS Nano 4 (12) (2010) 7151–7160.

[5] M. Estrader, A. López-Ortega, I.V. Golosovsky, S. Estradé, A.G. Roca, G. Salazar-Alvarez, L. López-Conesa, D. Tobia, E. Winkler, J.D. Ardisson, W.A.A. Macedo, A. Morphis, M. Vasilakaki, K.N. Trohidou, A. Gukasov, I. Mirebeau, O.L. Makarova, R.D. Zysler, F. Peiró, M.D. Baró, L. Bergström, J. Nogués, Origin of the large dispersion of magnetic properties in nanostructured oxides: Fe_xO/Fe_3O_4 nanoparticles as a case study, Nanoscale 7 (2015) 3002–3015.

[6] H. Chang, B.H. Kim, H.Y. Jeong, Continuous growth from iron-oxo clusters to iron oxide nanoparticles, J. Am. Chem. Soc. 141 (17) (2019) 7037–7045.

[7] I. Castellanos-Rubio, O. Arriortua, D. Iglesias-Rojas, A. Barón, I. Rodrigo, L. Marcano, J.S. Garitaonandia, I. Orue, M.L. Fdez-Gubieda, M. Insausti, A milestone in the chemical synthesis of Fe_3O_4 nanoparticles: unreported bulklike properties lead to a remarkable magnetic hyperthermia, Chem. Mater. 33 (22) (2021) 8693–8704.

[8] R. Hufschmid H. Arami, R.M. Ferguson, M. Gonzales, E. Teeman, L.N. Brush, N.D. Browning, K.M. Krishnan, Synthesis of phase-pure and monodisperse iron oxide nanoparticles by thermal decomposition, Nanoscale 7 (2015) 11142–11154.

[9] W.W. Yu, J.C. Falkner, C.T. Yavuz, V.L. Colvin, Synthesis of monodisperse iron oxidenanocrystals by thermal decomposition of iron carboxylate salts, Chem. Commun. (2004) 2306–2307.

[10] J. Park, K. An, Y. Hwang, Je-G. Park, H.-J. Noh, J.-Y. Kim, J.-H. Park, N.-M. Hwang, T. Hyeon, Ultra-large-scale syntheses of monodisperse nanocrystals, Nat. Mater. 3 (2004) 891–895.

[11] C. Erika, J. Vreeland, G.B. Watt, B.G. Schober, M.J. Hance, A.D. Austin, B.D. Price, T.C. Fellows, N.S. Monson, L. Hudak, A.C. Maldonado-Camargo, C. Bohorquez, C. Rinaldi, D.L. Huber, Enhanced nanoparticle size control by extending LaMer's mechanism, Chem. Mater. 27 (17) (2015) 6059–6066.

[12] S.J. Kemp, S.J. Kemp, R.M. Ferguson, A.P. Khandhar, K.M. Krishnan, Monodisperse magnetite nanoparticles with nearly ideal saturation magnetization, RSC Adv. 6 (2016), 77452.

[13] T. Iwamoto, T. Kinoshita, K. Takahashi, Growth mechanism and magnetic properties of magnetite nanoparticles during solution process, J. Solid State Chem. 237 (2016) 19–26.

[14] R. Chen, M.G. Christiansen, A. Sourakov, A. Mohr, Y. Matsumoto, S. Okada, A. Jasano, P. Anikeeva, High-performance ferrite nanoparticles through nonaqueous redox phase tuning, Nano Lett. 16 (2016) 1345–1351.

[15] B.H. Kim, K. Shin, S.G. Kwon, Y. Jang, H.S. Lee, H. Lee, S.W. Jun, J. Lee, S.Y. Han, Y.-H. Yim, D.-H. Kim, Sizes by weighinng: characterization sizes of ultrasmall-sized iron oxides nanocrystals using MALDI-TOF mass spectrometry, J. Am. Chem. Soc. 135 (2013) 2407.

[16] H. Kloust, R. Zierold, J.P. Merk, C. Schmidtke, A. Feld, E. Pöselt, A. Kornowski, K. Nielsch, H. Weller, Synthesis of iron oxide nanorods using a template mediated approach, Chem. Mater. 27 (2015) 4914–4917.

[17] A. Feld, A. Weimer, A. Kornowski, N. Winckelmans, J.-P. Merkl, H. Kloust, R. Zierold, C. Schmidtke, T. Schotten, M. Riedner, S. Bals, H. Weller, Chemistry of shape-controlled iron oxide nanocrystal formation, ACS Nano 13 (2019) 13.

[18] L.K. Plummer, J.E. Hutchison, Understanding the effects of iron precursor ligation and oxidation state leads to improved synthetic control for spinel iron oxide nanocrystals, Inorg. Chem. 59 (2020), 15074.

[19] A. Lak, D. Niculaes, G.C. Anyfantis, G. Bertoni, M.J. Barthel, S. Marras, M. Cassani, S. Nitti, A. Athanassiou, C. Giannini, et al., Facile transformation of FeO/Fe_3O_4 core-shell nanocubes to Fe_3O_4 via magnetic stimulation, Sci. Rep. 6 (2016) 1–12.

[20] I. Castellanos-Rubio, I. Rodrigo, R. Munshi, O. Arriortua, J.S. Garitaonandia, A. Martinez-Amesti, F. Plazaola, I. Orue, A. Pralle, M. Insausti, Outstanding heat loss via nano-octahedra above 20 Nm in size: from wustite-rich nanoparticles to magnetite single-crystals, Nanoscale 11 (2019) 16635–16649.

[21] L.M. Bronstein, X. Huang, J. Retrum, A. Schmucker, M. Pink, B.D. Stein, B. Dragnea, Influence of iron oleate complex structure on iron oxide nanoparticle formation, Chem. Mater. 19 (15) (2007) 3624–3632.

[22] G. Swiderski, M. Kalinowska, J. Malejko, W. Lewandowski, Spectroscopic (IR, Raman, UV and fluorescence) study on lhantanide complexes of picolinic acid, Vib. Spectrosc. 87 (2016) 81–87.

[23] H. Fjellvag, F. Gronvold, S. Stolen, B.C. Hauback, On the crystallographic and magnetic structures of nearly stoichiometric iron monoxide, J. Solid State Chem. 124 (1996) 52–57.

[24] M. Unni, A.M. Uhl, S. Savliwala, B.H. Savitzky, R. Dhavalikar, N. Garraud, D.P. Arnold, L.F. Kourkoutis, J.S. Andrew, C. Rinaldi, Thermal decomposition synthesis of iron oxide nanoparticles with diminished magnetic dead layer by controlled addition of oxygen, ACS Nano 11 (2017) 2284–2303.

[25] R.A. Harris, P.M. Shumbula, H. van der Walt, Analysis of the interaction of surfactants oleic acid and oleylamine with iron oxide nanoparticles through molecular mechanics modeling, Langmuir 31 (13) (2015) 3934–3943.

[26] I. Galarreta, M. Insausti, I. Gil de Muro, I. Ruiz de Larramendi, L. Lezama, Exploring reaction conditions to improve the magnetic response of cobalt-doped ferrite nanoparticles, Nanomaterials 8 (2018) 63.

[27] L. Qiao, Z. Fu, J. Li, J. Ghosen, M. Zeng, J. Stebbins, P.N. Prasad, M.T. Swihart, Standardizing size- and shape-controlled synthesis of monodisperse magnetite (Fe_3O_4) nanocrystals by identifying and exploiting effects of organic impurities, ACS Nano 11 (2017) 6370–6381.

[28] A. Muela, D. muñoz, R. Martín-Rodriguez, I. Orue, E. Garaio, A.A. Díaz de Cerio, J. Alonso, J.Á. García, M.L. Fdez-Gubieda, Optimal parameters optimal parameters for hyperthermia treatment using biomineralized magnetite nanoparticles: theoretical and experimental approach, J. Phys. Chem. C 120 (2016) 24437–24448.

[29] M.D. Carvalho, F. Henriques, L.P. Ferreira, M. Godinho, M.M. Cruz, Iron oxide nanoparticles: the Influence of synthesis method and size on composition and magnetic properties, J. Solid State Chem. 201 (2013) 144–152.

[30] E.C. Stoner, E.P. Wohlfarth, Phil. Trans. Math. Phys. Eng. Sci. 240 (826) (1948) 599–642.

[31] N. Guigue-Millot, N. Keller, P. Perriat, Evidence for the Verwey transition in in highly nonstoichiometric nanometric Fe-based ferrites, Phys. Rev. B Condens. Matter 64 (2001), 012402.

[32] V.A. Atsarkin, N. Noginova, Electron spin resonance on the border between para- and ferromagnetism: Quantum versus classical, Appl. Magn. Reson. 51 (2020) 1467–1480.

[33] I. Castellanos-Rubio, M. Insausti, E. Garaio, I. Gil de Muro, F. Plazaola, T. Rojo, L. Lezama, Fe_3O_4 nanoparticles prepared by the seeded growth route for hyperthermia: electron magnetic resonance as a key tool to evaluate size distribution in magnetic nanoparticles, Nanoscale 6 (2014) 7542.

[34] J. Salado, M. Insausti, L. Lezama, I. Gil de Muro, E. Goikolea, T. Rojo, Preparation and characterization of monodisperse Fe_3O_4 nanoparticles: an electron magnetic resonance study, Chem. Mater. 23 (2011) 2879–2885.